Contents lists available at ScienceDirect

# Materials Today Chemistry

journal homepage: www.journals.elsevier.com/materials-today-chemistry/





# Electron-phonon coupling dictates electron mean free paths and negative thermal diffusion in metals

Pravin Karna <sup>a</sup>, Md Rafiqul Islam <sup>b</sup>, Eric R. Hoglund <sup>c</sup>, Patrick E. Hopkins <sup>b,d,e</sup>, Ashutosh Giri <sup>a,\*</sup>

- <sup>a</sup> Department of Mechanical, Industrial and Systems Engineering University of Rhode Island, Kingston, RI, 02881, USA
- <sup>b</sup> Department of Mechanical and Aerospace Engineering University of Virginia, Charlottesville, VA, 22904, USA
- <sup>c</sup> Oak Ridge National Laboratory, Oak Ridge, TN, 37830, USA
- <sup>d</sup> Department of Materials Science and Engineering, University of Virginia, Charlottesville, VA, 22904, USA
- e Department of Physics, University of Virginia, Charlottesville, VA, 22904, USA

#### ARTICLE INFO

### Keywords: Negative thermal diffusion Pump-probe spectroscopy Electron-phonon coupling factor Electron diffusion

#### ABSTRACT

The spatiotemporal dynamics of the fundamental energy carriers in metals underpin the efficiency of a wide array of technologies. Although much progress in our understanding of the temporal response of electronic relaxation processes following an external field perturbation has been achieved, the spatial relaxation dynamics of electrons after excitation remains unclear. Here, we employ a scanning ultrafast microscopy with high spatial resolution to directly measure the mean free paths of electrons in different metals. We show that the strength of electron-phonon coupling not only dictates the mean free paths, but also controls a peculiar spatial shrinking of the electronic temperature profile immediately after the electrons have thermalized with the 'colder' lattice. More specifically, from our experimental tracking of the spatial relaxation profiles, a clear observation of an effective negative thermal diffusion is apparent for metals with weaker electron-phonon coupling, while for metals with stronger electron-phonon coupling, the negative thermal diffusion effect is not observable. Our spatiotemporal modeling based on the two-temperature approach provides evidence that although negative diffusion occurs universally for materials with two different species that have varying diffusivities and are thermodynamically coupled, effective negative diffusion is masked for cases with stronger coupling between the species.

## 1. Introduction

The fundamental scattering mechanisms of electrons with phonons in metals are significant to various phenomena in materials science including spintronics [1,2], superconductivity [3,4], plasmon resonances [5], drastic modification of the dielectric, optical, electrical, and thermal transport properties [6–9], laser induced phase transitions and nonthermal melting [10–13] to name a few. Likewise, it also underpins the progress in a wide array of applications ranging from determining the proper functionality of interconnect lines in integrated circuits [14, 15], to dictating the efficiencies of plasmonic devices [16–18], photovoltaics [18,19], nonlinear optics and photocatalysis [20,21]. As such, dating back to 1900 when the seminal work by Drude described the scattering processes of a free electron gas [22], a considerable amount of work has been undertaken towards understanding the electron-phonon scattering processes in metals.

Experimentally, the conventional approach has mostly relied upon time-resolved ultrafast pump-probe measurements [23-32], which have revealed critical processes involving the relaxation of photo-excited electrons with the colder lattice that occur within a few picoseconds. Owing to their vastly reduced heat capacities as compared to the metallic lattice, electrons first gain the photon energies and thermalize within themselves to create a Fermi-Dirac distribution via electron-electron collisions before any substantial relaxation occurs with the 'colder' lattice. Although these energy relaxation pathways are seemingly straightforward, the absorption of femtosecond laser pulses has been associated with a cascade of nonequilibrium kinetics such as, non-Fermi distributions [33-35], ballistic electron transport [25,36], photoemission [37-39], plasmon resonances [40-42], nonthermal melting [12,43,44], large changes in the microstructure and thermo-mechanical responses at the surface due to large temperature gradients [13,45-47], and drastic modification of the dielectric [48,49],

E-mail address: ashgiri@uri.edu (A. Giri).

 $<sup>^{\</sup>ast}$  Corresponding author.

and optical properties [50]. In all of these processes, electron-phonon thermalization plays a significant role in dictating the evolution of the nonequilibrium kinetics.

These prior studies have substantially advanced our knowledge of the temporal evolution of the electron relaxation processes in metals. However, they provide little information about the spatial relaxation dynamics of hot carriers, thus leaving a gaping void in our understanding of critical processes and key information such as the direct experimental quantifications of the mean free paths of electrons, which are crucially needed to validate recent theoretical calculations [14,16]. To fill this void, some recent studies have utilized spatially resolved pump-probe experiments with diffraction-limited spots to investigate the spatial relaxation processes in various 2D transition metal chalcogenides to study excitons dynamics [51,52], in hybrid perovskites to unravel hot carrier transport [53-55], and in nanowires and atomically thin heterostructures to uncover trap states and charge transfer transitions [56-58]. For metals, however, spatially resolved measurements have only been limited to thin gold films [59-61]. These studies have provided critical insights into the spatiotemporal dynamics of photo-excited electrons such as the identification of a rapid diffusion regime immediately after laser excitation, followed by a 100-fold slower diffusion at longer time scales [59-61]. Most notably, through these experiments, accurate measurements of in-plane thermal conductivity of the thin films [60,61], along with the determination of ballistic electron length scales of >150 nm in gold thin films have been made possible [61].

In this work, we use ultrafast pump-probe microscopy with high spatial resolutions to track the dynamics of electrons in real time and space for four different metals with varying band structures: we study aluminum (the prototypical free-electron metal), gold and copper (which are noble metals) and tungsten (a transition metal). With the high spatiotemporal resolutions, we measure average diffusive electron mean free paths of the metals, which agree very well with the results from our parameter-free density functional theory calculations of the full electron-phonon coupling matrix. From our ultrafast thermal diffusion measurements, after the electron-phonon relaxation and before the longer time thermal diffusion, we observe signatures of pronounced contraction of thermal diffusion in Au and Cu, while Al and W do not demonstrate such signatures of negative thermal diffusion in their spatially resolved thermoreflectance measurements. By utilizing the two-temperature approach, we show that during this intermediate time period, the electronic temperature drops below the phonon temperature in the region that is locally heated by the laser leading to the effective negative thermal diffusion. Our calculations show that such transient shrinkage of the electron temperature in space (or the negative thermal diffusion) in metals could be a universal phenomenon for systems with two species that have drastically different diffusivities (as also discussed

by Block *et al.* [62] from their measurements on a gold thin film with a similar pump-probe technique). Moreover, we also show that the magnitude of the negative thermal diffusion is highly dependent on the strength of the coupling between the two diffusing species. Finally, our extensive calculations of the electron-phonon coupling factor for the different metals show that along with the negative thermal diffusion, the diffusive mean free paths of electrons are also highly dependent on the electron-phonon coupling strength in the metals.

## 2. Results and discissions

Our spatial tracking of the electron dynamics in the metals is performed using our home-built ultrafast super-resolution thermore-flectance microscopy. This technique is capable of exciting the samples at one location with a pump beam and monitoring the transport of energy carrier diffusion at a different location with a probe beam (as schematically shown in Fig. 1a). More importantly, the separation between the diffraction-limited laser spots can be controlled with nanometric spatial resolutions and thus allows us to directly visualize the carrier motion with

the spatially separated pump-probe images acquired for a range of delay times between the two pulses. A more detailed description of the experimental setup is given in the methods section. We use polycrystalline metallic thin films with grain sizes that are larger than the average mean free path of electrons in these metals as shown in Fig. S5 of the Supplemental Information. A characteristic spatiotemporal mapping of energy relaxation process conducted on our copper thin film is shown in Fig. 1b. Initially, right after short-pulse excitation, the electrons are perturbed to a non-Fermi distribution, which relaxes via electronelectron scattering to a Fermi distribution within tens to hundreds of femtoseconds [33]. The electrons at elevated temperature with excess energy couple rapidly with the lattice in several picoseconds before a slower thermal diffusion process carries the heat away from the locally heated spot on the sample. To gain insights into these diffusion processes occurring in the thin metal films, we obtain Gaussian profiles (from  $\Delta$ R/R measurements as shown in Fig. 1c for our copper film) from the spatial mapping at various pump-probe delay times. Note,  $\Delta R/R$  represents the normalized change in reflectivity with respect to the maximum reflectivity obtained for our various metallic films. From these Gaussian profiles, we can extract the full-width at half maximum  $(\sigma)$ , which provides information on the spatial diffusion of thermal energy on the sample surface; the slope of  $\sigma^2$  plotted as a function of pump-probe delay time is a measure of the thermal diffusivity (see Section S3 of Supplemental Information).

We present our results from the measurements on the different metals with our ultrafast super-resolution thermoreflectance microscopy in Fig. 2. We observe two diffusion regimes for all metals: a rapid

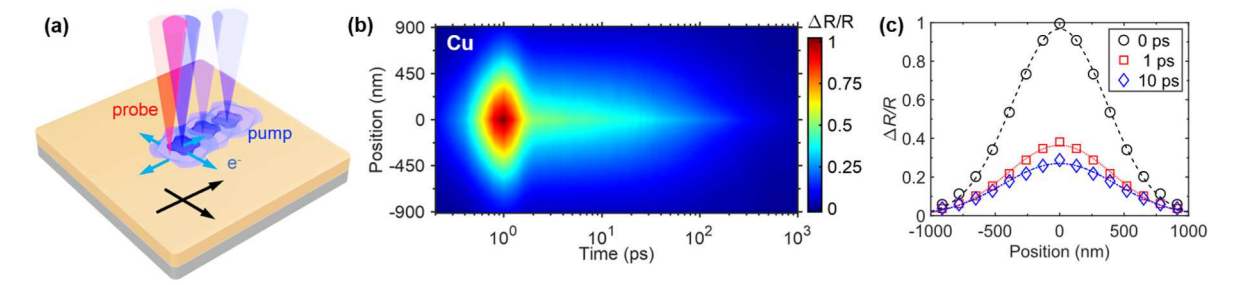


Fig. 1. Spatial tracking of electron relaxation through scanning ultrafast microscopy. Schematic of the ultrafast super-resolution thermoreflectance technique demonstrating the unique capability to offset a diffraction-limited pump along a scan axis while the stationary probe interrogates the response from the pump-induced changes on the sample surface. (b) Characteristic contour showing the spatiotemporal profiles obtained with nanometric precision for a 500 nm thick Cu film. The spatiotemporal profiles at early time delays (before the electrons couple with the phonons) are mainly dictated by the electronic temperature. However, the spatiotemporal profiles after the electrons have coupled with the phonons are dictated by both the electronic and phononic subsystems that are in equilibrium. (c) Monitoring the Gaussian profiles of the reflected probe at various pump-probe time-delays provides insights into the energy carrier diffusion processes. The term  $\Delta R/R$  represents the normalized change in reflectivity with respect to the maximum reflectivity.

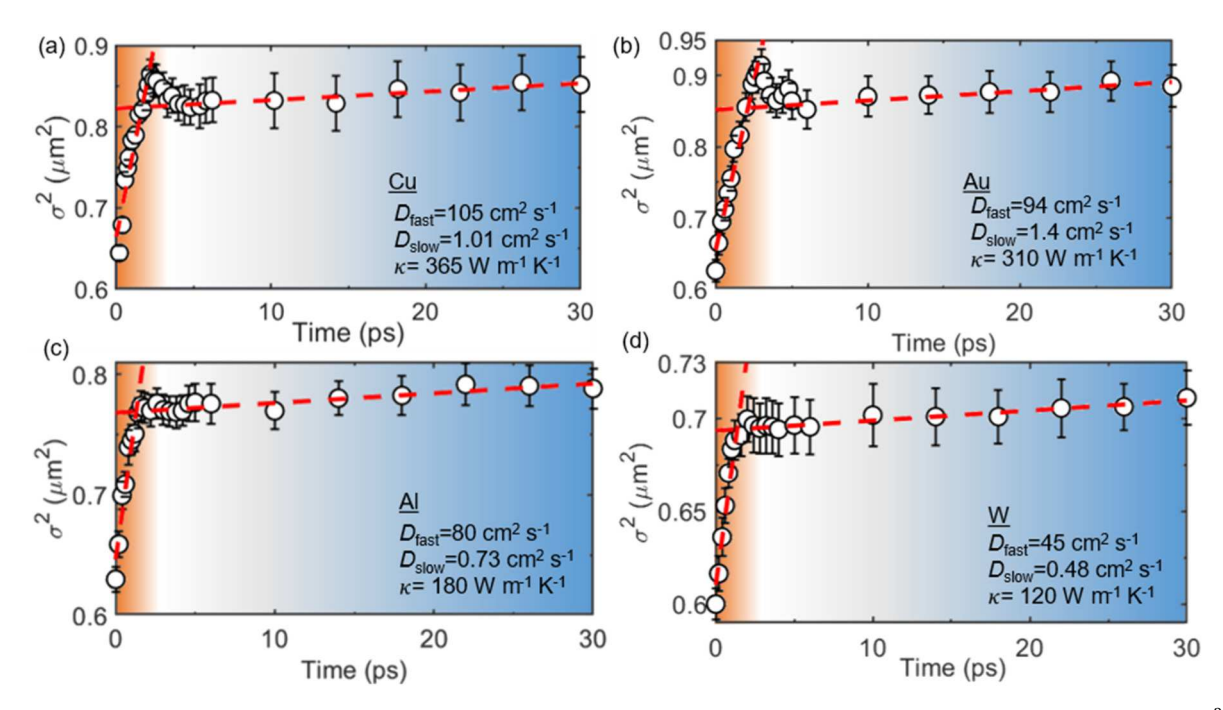


Fig. 2. Demonstration of negative thermal diffusion in metals with weak electron-phonon coupling. Square of the full-width at half maximum ( $\sigma^2$ ) obtained from the Gaussian profiles at various pump-probe time-delays for thin films of (a) Cu, (b) Au, (c) Al and (d) W. The slope of  $\sigma^2$  is related to the thermal diffusivity. For all metals, we observe a fast and a slow diffusion regime. The fast diffusion regime is related to the equilibration of **photo-excited electrons** that couple with the 'cooler' lattice, whereas in the slower diffusion regime the electrons and phonons are in thermal equilibrium. For the noble metals (Cu and Au), an effective negative diffusion appears at the intermediate time regime. This peculiar negative diffusion is related to the spatial shrinking of the electrons, whereby they move back towards the excitation center right after coupling with the 'cooler' lattice. This phenomenon is not observable for Al and W, which we attribute to the strong electron-phonon coupling in these metals in comparison to the weaker coupling in the Cu and Au films.

initial regime for the first couple of picoseconds followed by a much slower regime on the longer time scale. The diffusion coefficients obtained for these two regimes are listed in Table 1 for all four metals. For the longer-time (slow diffusion) regime, when the electrons and phonons in the metals are in equilibrium, we can estimate the thermal diffusivity as,  $D_{slow} = \kappa_{total}/(C_e + C_p)$ , where  $\kappa_{total} = \kappa_e + \kappa_p$ ;  $\kappa_e$  and  $\kappa_p$  are the electron and phonon thermal conductivities, respectively. Similarly,  $C_{\rm e}$  and  $C_{\rm p}$  are the electron and phonon heat capacities, respectively. The values of  $\kappa_{total}$  we obtain for the thin films (including their respective thicknesses) are also listed in Table 1, which are in good agreement with prior literature values [60,63]. We note that, although the film thicknesses of these metallic films are different, the thicknesses are greater than the average electron mean free paths of these metals [14,64,65], which avoids the effect of electron-boundary scattering on the measured thermal conductivities. The lattice heating effect due to laser irradiation could also influence the lattice thermal conductivities of the metallic thin films. In this regard,  $\kappa_p$  values of 2.6 W m<sup>-1</sup> K<sup>-1</sup> for gold [66], 7.25 W m $^{-1}$  K $^{-1}$  for copper [67], 6 W m $^{-1}$  K $^{-1}$  for aluminum [66] and  $\sim$ 40–60 W m<sup>-1</sup> K<sup>-1</sup> in tungsten [65,68] have been predicted through first-principles-based calculations at room temperature. As such, we can safely ignore the effect of lattice heating on the thermal properties of the free-electron-like metals with negligible contributions from the phonons to the total thermal conductivity. However, for tungsten, the substantial

contribution from the lattice could be influenced by the lattice heating effect due to laser irradiation, which would help explain the slight discrepancy between our measurements (see Table 1) and the value of 154 W  $\rm m^{-1}~K^{-1}$  reported in prior literature [69]. This shows that our ultrafast super-resolution thermoreflectance microscopy provides a robust approach to measure the in-plane thermal conductivities of thin films by tracking the variation of thermoreflectance on the thin film surface with high spatial resolutions.

For the fast diffusion regime, when the electrons are mainly out of equilibrium with the phonons, we can estimate the electronic diffusivities for the metals by the relation  $D_{fast} = \kappa_{\rm e}/C_{\rm e}$ . From this relationship, we can estimate the average diffusive mean free path of electrons with the knowledge of their respective Fermi velocities,  $\nu_{\rm F}$ , as determined from our density functional theory (DFT) calculations, which are also listed in Table 1. For comparison, we also list our predictions of the average mean free paths of electrons at the Fermi energy calculated fully from first-principles in Table 1. The details of our first-principles calculations and the calculation of electron scattering rates for all metals are given in the methods section. It could be expected that the mean free path of electrons could change due to the strong nonequilibrium conditions imposed immediately after laser irradiation. In this regard, prior work based on density functional perturbation theory (DFPT) has shown that the change in the average mean free path of electrons in gold is

Table 1
The values of metal film thicknesses, diffusivities of the slow ( $D_{\rm slow}$ ) and fast regime  $D_{\rm fast}$ , experimentally measured thermal conductivities of the films ( $\kappa_{\rm total}$ ), first-principles calculated average Fermi velocities ( $\nu_{\rm F}$ ), experimentally measured and DFT-predicted average mean free paths of diffusive electrons ( $\Lambda_{\rm exp}$  and  $\Lambda_{\rm DFT}$ , respectively), and first-principles-based calculations of the volumetric electron-phonon coupling factor (G) for the four metals.

Metal	Thickness (nm)	$D_{\rm fast}~({\rm cm}^2{\rm s}^{-1})$	$D_{\rm slow}~({\rm cm}^2{\rm s}^{-1})$	$\kappa_{\text{total}} \; (\text{Wm}^{-1} \text{K}^{-1})$	$v_{\rm F}~(10^6~{\rm ms}^{-1})$	$\Lambda_{\rm exp}$ (nm)	$\Lambda_{DFT}$ (nm)	$G_{calc}$ (Wm <sup>-3</sup> K <sup>-1</sup> )
Cu	500	105	1.01	$360 \pm \! 40$	1.13	43 ±7	19	$8.0\times10^{16}$
Au	200	94	1.4	$310\pm40$	1.35	42 ±7	37	$2.2\times10^{16}$
Al	70	80	0.73	$180 \pm 30$	1.6	$23 \pm 4$	19	$4.5 \times 10^{17}$
W	30	45	0.48	$120\; {\pm}20$	0.94	$21~{\pm}4$	16	$2.2\times10^{17}$

negligible for electron temperatures of up to  $\sim\!10,\!000$  K [8]. Our analysis of two temperature picture shows that for the pump fluences used, the maximum electron temperatures reached are  $\sim\!3,\!800$  K for Au, which is well below the electron temperature when one could expect the mean free paths of electrons to change substantially.

Our experimentally determined average mean free paths ( $\Lambda_{exp}$ ) agree well with our DFT calculations for all metals providing confidence in our measurements. Note, our approach of fitting the fast diffusion regime is sensitive to our choice of  $\Lambda_{exp}$  as shown in Fig. S7 of the Supplementary Information, thus allowing for its' accurate measurements within 15% uncertainties. The noble metals (Cu and Au), possess the longer mean free paths, and as a consequence, have higher thermal conductivities as compared to Al and W. We will attempt to understand this in greater depth by analyzing our results in the following discussions.

In metals, electron-phonon coupling (the strength of which is described by the mass enhancement parameter,  $\lambda$ ) is the dominant mechanism that drives both the fast and the slow diffusion regimes observed in our experiments. Therefore, to understand the origins of the varying electron mean free paths obtained in our experiments, we perform calculations of the full electron-phonon coupling matrix to reveal the phonon linewidths from electron-phonon scattering as determined by our parameter-free DFPT calculations. Fig. 3a–d shows the phonon linewidths along the high symmetry directions and the Eliashberg spectral function,  $\alpha^2 F(\omega)$ , which is used to calculate the overall

electron-phonon coupling strength, 
$$\lambda=2\int\limits_{0}^{\infty}\left( \alpha^{2}F(\omega)\left/ \omega\right) d\omega$$
 for all four

metals. Note, our calculations of  $\lambda$  (as listed in Table 1) match well with the results from prior works [66,70,71]. The noteworthy aspect of the calculations presented in Fig. 3a–d is that the lower frequency (long wavelength) acoustic phonons in noble metals with the weaker electron-phonon coupling contribute significantly to the overall  $\lambda$  as compared to Al and W; the higher frequency longitudinal acoustic phonons in Al and W contribute more towards electron-phonon coupling as demonstrated by their linewidths and the spectral functions. This fact, along with the variations in the electronic density of states (see Fig. S15) helps explain the varying strengths of electron-phonon coupling between the different metals.

From our DFT calculations, we also determine the volumetric electron-phonon coupling factor, G, that is generally measured with ultrafast pump-probe measurements [23,28,72–75] and is given as [76],

$$G = \pi \hbar k_B \langle \omega^2 \rangle \int_0^\infty \frac{(D(\varepsilon))^2}{D(\varepsilon_F)} \left[ -\frac{df}{d\varepsilon} \right] d\varepsilon \tag{1}$$

here  $\omega^2$  is the second moment of the phonon spectrum and  $D(\varepsilon)$  represents the electronic density of states [77]. By plotting the mean free paths as a function of G as shown in Fig. 3e, where solid symbols represent our measured  $\Lambda$  and the open symbols represent results from our DFT-based calculations, we find that metals with larger values of G possess shorter mean free paths. Note, we have performed additional calculations on Ru, Mo and Nb, which have stronger electron-phonon coupling along with Ag, which has the weakest electron-phonon coupling among all metals as shown in Fig. 3e. This analysis shows that stronger electron-phonon coupling results in shorter mean free paths in metals, which is intuitive since stronger electron-phonon coupling results in higher electron scattering rates (Fig. S16).

We now turn our focus to the intermediate time regime (between the fast and the slow diffusion regimes) where we observe considerable decrease in  $\sigma^2$  for the noble metals, which is absent from the data taken for Al and W (Fig. 2). This decrease is indicative of a negative thermal diffusion, where the electron temperature spot spatially shrinks and moves back towards the excitation center right after coupling with the 'cooler' lattice. We note that such a negative diffusion in spatially resolved pump-probe measurements has recently also been identified for excitons in monolayer transition metal dichalcogenides [78] and single-crystal tetracene [79] albeit in the picosecond and nanosecond timeframes, respectively. This has also been previously observed in thin gold films (including our prior work) [60,61,62]. However, the intrinsic mechanism controlling such an anomalous negative diffusion has not been comprehensively understood, which is what we focus on in the following discussions.

To understand this mechanism, we turn to the widely used twotemperature approach [23],

$$C_{\rm e}(T_{\rm e})\frac{\partial T_{\rm e}}{\partial t} = \nabla \cdot (\kappa_{\rm e} \nabla T_{\rm e}) - G(T_{\rm e} - T_{\rm p}) + S(t)$$
(2)

$$C_{\rm p}(T_{\rm p})\frac{\partial T_{\rm p}}{\partial t} = \nabla \cdot (\kappa_{\rm p} \nabla T_{\rm p}) - G(T_{\rm e} - T_{\rm p}),$$

where  $T_{\rm e}$  and  $T_{\rm p}$  are the electronic and lattice temperatures, respectively, and S(t) is the laser source term. This two-temperature picture

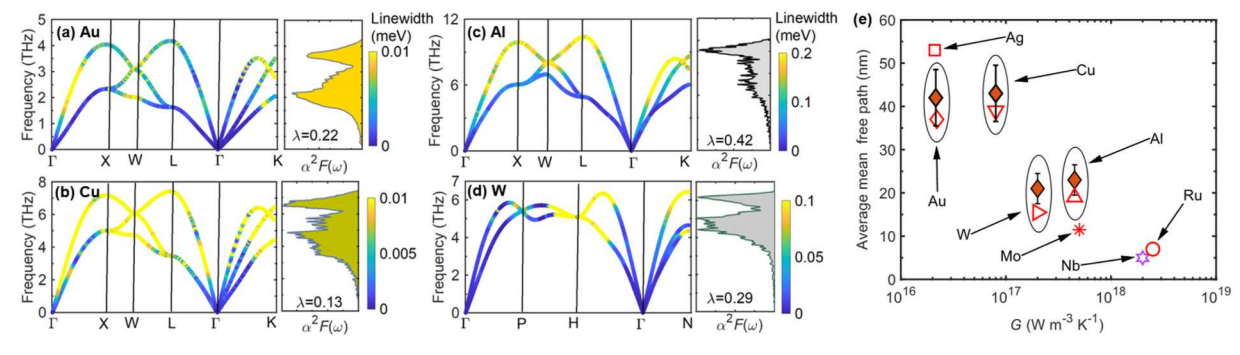


**Fig. 3. Influence of the strength of electron-phonon coupling on the mean free paths of electrons in metals.** Density functional perturbation theory calculated phonon dispersions along several high symmetry directions for (a) Au, (b) Cu, (c) Al and (d) W, where the color intensities of the phonon branches indicate the linewidths ( $\gamma = \hbar/\tau$  or the imaginary part of the phonon self-energy that is related to the lifetimes,  $\tau$ , of the individual phonon modes) due to electron-phonon interactions. The corresponding mass enhancement parameters,  $\lambda$ , and the Eliashberg spectral functions,  $\alpha^2 F(\omega)$ , representing the overall strength of electron-phonon coupling in the metals are also shown. The metals (Au and Cu) have relatively weaker electron-phonon coupling as compared to Al and W, for which higher frequency modes in the phonon spectrum contribute more towards the coupling. Moreover, although Al has the same face-centered cubic structure as the noble metals, higher frequency longitudinal modes scatter more with the electrons, thus resulting in higher values of  $\lambda$ . (e) Average mean free paths of electrons as a function of the volumetric electron-phonon coupling factor, G, for various metals. The solid symbols represent our experimental measurements of the mean free paths obtained from the fast diffusion regime in Fig. 2. The hollow symbols along with the values of G for the various metals are from our first-principles calculations. For metals with low values of G, the mean free paths are longer, which shows the strong role played by electron-phonon scattering in dictating the spatial relaxation length scales of electrons. (For interpretation of the references to color in this figure legend, the reader is referred to the Web version of this article.)

formulation has been extensively used to interpret time-resolved experiments based on pump-probe spectroscopies [23,28,72-75]. We conduct calculations for Cu as shown in Fig. 4a, where the negative thermal diffusion is well captured by the two-temperature picture. By fictitiously varying G, we observe substantial (and monotonic) decrease in the negative thermal diffusion with increasing values of G. Indeed, we do not observe the characteristic negative diffusion in our experimental results for Al and W (Fig. 1c and d, respectively) both of which have high values of G (Table 1). Therefore, the strength of electron-phonon coupling not only dictates the diffusive mean free paths of electrons, but also controls the extent to which electrons experience negative effective thermal diffusion (or shrinking of the spatial electronic temperature profiles) following electron-phonon relaxation. We note that for longer time scales (beyond ~10 ps) phonon-phonon scattering could be playing a role in dictating the thermal diffusion process mainly in metals with substantial contribution from the phononic subsystem to the heat conduction (such as in tungsten). However, for the timescales associated with the negative diffusion (~2.5 ps, which is immediately after electrons have coupled with phonons), we can safely assume that phonon-phonon scattering does not influence the shrinking of the electronic temperature profiles.

To further understand the negative thermal diffusion, we separate the contributions from the influence of electron-phonon coupling term  $(A_1 = T_{\rm e} - T_{\rm p})$  and the electron heat diffusion term  $(A_2 = -(\kappa_{\rm e}/G)\nabla^2T_{\rm e})$  in the two-temperature picture (as carried out in ref. [62]). The results of the calculations are shown in Fig. 4b for Cu and W, representing the metals with low and high values of G, respectively. Note, throughout these calculations, we use constant value of G for the entire nonequilibrium time regime for both Cu and W. However, as shown by prior works [8,16,76], G can vary significantly with electron temperature during this timeframe. We note that using a temperature dependent G for these calculations can significantly increase the complexity of the

analysis. However, as our main goal is to understand the effect of varying G on the negative thermal diffusion, we do not expect the conclusions to change based on the use of a temperature dependent  $G(T_{\rm e})$ . A positive value corresponds to a decrease in the local electron temperature at different pump-probe delay times for both terms. Initially, right after laser excitation (0.3 ps),  $A_1$  is positive across the whole spatial extent (as shown for Cu in Fig. 4c and in Fig. S9 for W). However, the diffusion term is negative away from the center, which indicates the electronic heat conduction occurs away from the center broadening the spatial temperature profiles. Although this occurs for both metals, it is more pronounced in Cu with the weaker electron-phonon coupling. At the time regime of the negative diffusion immediately after the electrons have coupled with the lattice (5 ps in Cu and 2.5 ps in W), the electron-phonon coupling term  $(A_1)$  no longer has its maximum at the center and the electrons couple more at locations away from the center (Fig. 4d), thus leading to a negative effective diffusion and shrinking of the temperature profile. The 'dip' in the center location of the  $A_1$  persists long after electron-phonon equilibration and attains a negative value (as shown in Fig. S9) at longer time scales, leading to phonon temperatures exceeding those of electrons at the center (Fig. S8). While this is also the case for W, the maximum temperatures associated with the electron-phonon coupling term  $(A_1)$  are comparatively much less pronounced in W than in Cu (Fig. 4e). This shows that the negative effective diffusion is not intrinsic to noble metals or metals with weak electron-phonon coupling but is a more general phenomena occurring when two species with different diffusivities (namely electrons and phonons in metals or fast and slow excitons in various semiconductors [78,79] couple with each other as they diffuse in the material. However, when the coupling is strong between the two species, the negative effective diffusion effect is masked and might not be evidently observed in experiments that spatially track their dynamics.

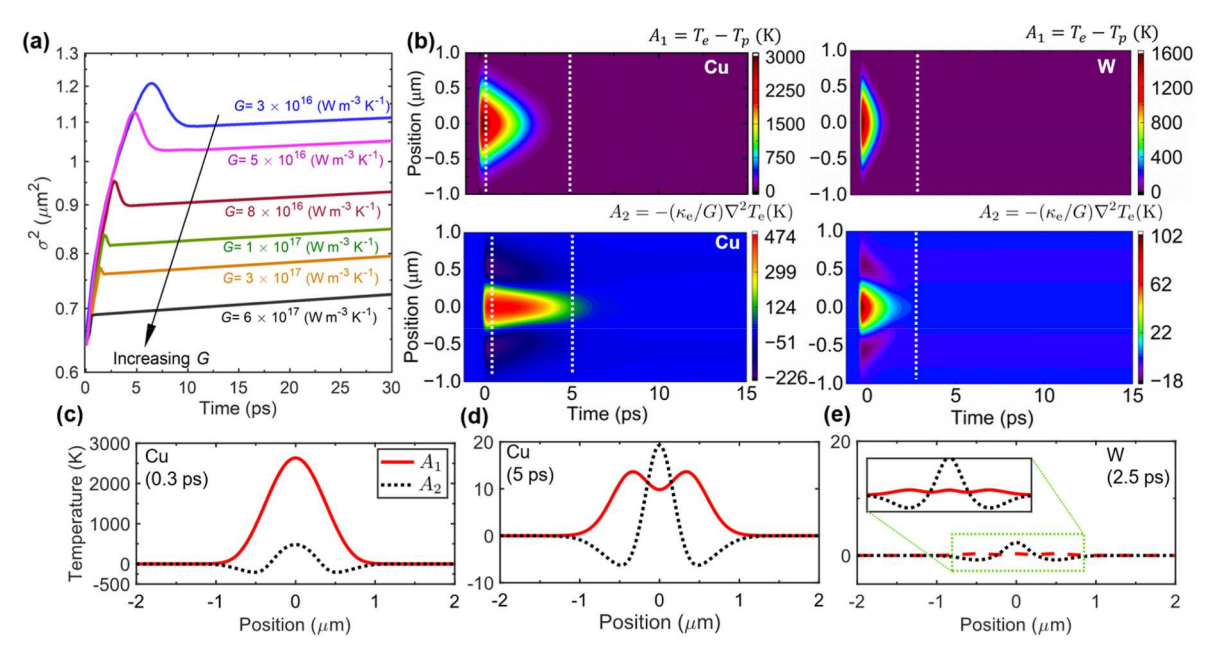


Fig. 4. Influence of the strength of electron-phonon coupling on the negative thermal diffusion. (a) Two-temperature picture-based calculations of thermal diffusion for electrons in Cu, where we have systematically (and fictitiously) varied G to gain insight into the role of electron-phonon coupling in dictating the negative thermal diffusion observed in our experiments conducted on the noble metals. As G is increased, the 'hump' representing the effective negative diffusion of the electron temperature monotonically decreases, highlighting the strong role of electron-phonon coupling in dictating the spatial shrinkage of the electrons towards the excitation center. (b) Spatiotemporal profiles of the two terms representing electron-phonon coupling  $(A_1 = T_e - T_p)$  and electron heat diffusion  $(A_2 = -(\kappa_e/G)\nabla^2 T_e)$  in the two-temperature picture for Cu (that has a weaker electron-phonon coupling) and W (that has a relatively stronger electron-phonon coupling). (c) Spatial profiles of the two terms at selected time-delays as shown by the vertical dashed lines in (b). The progressive shift of  $A_1$  away from the center after electron-phonon equilibration is responsible for the effective negative diffusion. While this phenomena is universal for materials with two diffusing species that are thermodynamically coupled (as shown in the inset for W), the strong coupling can mask this effect, thus leading to the absence of the pronounced 'hump' that is representative of effective negative diffusion.

#### 3. Conclusions

In summary, we have employed our home-built ultrafast microscopy to interrogate the spatiotemporal response of thermal diffusion in representative metallic films of Au and Cu (which are noble metals), Al (which is a free-electron-like metal) and W (a transition metal). Our measurements reveal that for all four metals, a fast diffusion regime followed by a 100-fold slower thermal diffusion process, after laser excitation, carries the heat away from the excitation center. From the slower diffusion process, it is possible to accurately measure the in-plane thermal conductivities of the thin films with our approach. From the fast regime, we can also measure the average diffusive mean free paths of electrons in the four different metals, which agree very well with our first-principles calculations. From our extensive and parameter-free density functional theory calculations, we find that metals with stronger electron-phonon coupling possess shorter mean free paths for electrons; noble metals with relatively weak electron-phonon coupling have characteristic mean free paths that are upwards of 40 nm at room temperature. Our experimental measurements on the noble metals also reveal a peculiar negative diffusion regime immediately following the coupling of electrons with the 'colder' lattice, whereby the electronic temperature profile shrinks in space, moving towards the excitation center rather than diffusing outwards as would be typically expected for heat diffusion. This phenomenon, although not clearly observable in Al and W from our super-resolution thermoreflectance measurements, is shown to be a universal feature of materials with two species that have varying diffusivities [62].

### 4. Experimental section/methods

# 4.1. Experimental details

The experimental setup shown in Fig. S1 is based on a Ti:Sapphire laser emitting ultrafast (100 fs) pulses centered at 800 nm with a repetition rate of 80 MHz. These pulses are split with a beam splitter into two paths: the pump and the probe paths. The pump beam is modulated at 10 MHz using an electro-optic modulator (Conoptics, 350-160-02), while the probe beam's arrival time is precisely delayed with respect to the pump beam by a computer-controlled mechanical delay stage (Newport-M-360-90). To initiate the specific electronic transitions in the metallic thin films, the pump beam undergoes frequency doubling from 1.55 eV to 3.11 eV. The probe beam is divided into a reference arm using a non-polarizing beam splitter, enabling balanced photodetection and reduced noise. Both the pump and the probe beams are directed at the sample through a dichroic mirror, with microscope objective of  $100 \times \text{magnification}$  used for focusing with diffraction-limited spot onto the sample surface.

We use the knife edge method to measure  $1/e^2$  radii of the pump and the probe spots to be 0.65 and 0.55  $\mu$ m, respectively as shown in Fig. S2. The stationary probe beam allows us to investigate the sample's optical response while the pump beam is scanned along the *x*-axis by controlling the dichroic mirror with nanometric precision. This movement is controlled by a picometer controller (New Focus Picomotor Controller/ Driver, Model 8742) integrated with a mirror mount (New Focus 8821), providing nanometric resolution (of ~20 nm) for accurate positioning. This setup facilitates ultrafast pump-probe microscopy, enabling us to study ultrafast spatial dynamics and transient processes in materials at the microscopic level. The synchronized laser pulses and adjustable time-delays offer valuable insights into the sample's thermoreflecatnce response under pump excitation. For these measurements, we vary the pump fluences in the range of 1-3 mJ cm $^{-2}$  to make sure our results are not influenced by the choice of our fluence. We keep the probe fluence below 1 mJ cm<sup>-2</sup> for all of our measurements.

### 4.2. First principles calculations: methodology

The calculation of electron-phonon matrix elements involves the use of Electron Phonon Wannier (EPW), which is integrated with the Quantum Espresso package [80]. The Eliashberg spectral function,  $\alpha^2 F$  ( $\omega$ ), describes the strength of electron-phonon coupling for each phonon mode and is given as [81].

$$\alpha^{2}F(\omega) = \frac{1}{2} \sum_{\nu} \int_{\omega} \frac{d\mathbf{q}}{\Omega_{BZ}} \omega_{\mathbf{q}\nu} \lambda_{\mathbf{q}\nu} \delta(\omega - \omega_{\mathbf{q}\nu})$$
(3)

where  $\nu$  represents the branch index of the phonon wave vector  $\mathbf{q}$  with associated frequency  $\omega_{\mathbf{q}\nu}$ ,  $\Omega_{BZ}$  is the volume of the Brillouin zone,  $\delta$  is a small positive parameter to ensure the correct analytical structure of the self-energies.  $\lambda_{\mathbf{q}\nu}$  is the electron-phonon coupling strength associated with a specific mode  $\nu$  and wave vector  $\mathbf{q}$  and is given as,

$$\lambda_{qv} = \frac{1}{N(\varepsilon_F)\omega_{\mathbf{q}v}} \sum_{nm} \int_{BZ} \frac{d\mathbf{k}}{\Omega_{BZ}} \times |g_{mn,v}(\mathbf{k}, \mathbf{q})|^2 \delta(\varepsilon_{n\mathbf{k}} - \varepsilon_F) \delta(\varepsilon_{m\mathbf{k}+q} - \varepsilon_F)$$
(4)

where  $N\left(\varepsilon_{\mathrm{F}}\right)$  denotes the density of states of electrons at the Fermi level,  $g_{mn,v}\left(\mathbf{k},\mathbf{q}\right)$  represents the electron-phonon matrix elements that describe the scattering of an electron at the Fermi surface from the state  $n\mathbf{k}$  to the state  $m\mathbf{k}+\mathbf{q}$ , where  $\mathbf{k}$  is the electron wave vector. The total electron-phonon coupling parameter  $\lambda$ , which quantifies the overall strength of electron-phonon coupling is calculated as the Brillouin zone average of the mode-resolved coupling strengths  $\lambda_{\mathbf{q}v}$ ,

$$\lambda = \sum_{\mathbf{q}_{\nu}} \omega_{\mathbf{q}} \lambda_{\mathbf{q}_{\nu}} \tag{5}$$

where  $\omega_{\mathbf{q}}$  are the Brillouin zone weights associated with the phonon wave vectors  $\mathbf{q}$ , normalized to 1 in the Brillouin zone. To ensure the accurate calculation of Eq. S8, dense meshes of k and q grids in the Brillouin zone are essential. This is achieved by interpolating the electron-phonon matrix elements, phonon modes, and band energies from an initial coarse grid (10  $\times$  10  $\times$  10 and 5  $\times$  5  $\times$  5) to a uniform fine grid (80  $\times$  80  $\times$  80 and 35  $\times$  35  $\times$  35) for electron and phonon wavevector grids, respectively. The interpolation employs maximally localized Wannier functions derived from the Bloch energy bands [82]. For these calculations, norm-conserving pseudopotentials are used for Cu, Au, Ag and Mo taken from the PS Library [83]. These calculations employ the Perdew-Burke-Ernzerhof (PBE) functionals of the generalized gradient approximation. For Al, W and Nb, we use norm-conserving, non-relativistic pseudopotential with Perdew-Zunger (LDA) exchange correlation functional. We implement a plane wave cutoff of 1632.7 eV (120 Ry) for these calculations.

The accuracy and convergence of the Wannier interpolation can be confirmed by the spatial decays of the Hamiltonian, the dynamical matrix, and the electron-phonon coupling matrix, which should converge towards zero. The calculated Hamiltonian is given by,

$$H_{\mathbf{R}_{e},\mathbf{R}_{e}^{\cdot}}^{\mathrm{el}} = \sum_{\mathbf{k}} \omega_{\mathbf{k}} e^{-i\mathbf{k}\cdot\left(\mathbf{R}_{e}^{\cdot}-\mathbf{R}_{e}\right)} U_{\mathbf{k}}^{\dagger} H_{\mathbf{k}}^{el} U_{\mathbf{k}}$$

$$\tag{6}$$

here,  $w_k$  represents the weight of k points,  $R_e$  denotes the electron unit cell, and the gauge matrix  $U_k$  relates the Bloch eigenstates to the maximally localized functions. The transformation of the dynamical matrix to real-space is performed using:

$$D_{\mathbf{R}_{p},\mathbf{R}_{p}^{-}}^{\mathrm{ph}} = \sum_{\mathbf{q}} \omega_{\mathbf{q}} e^{-i\mathbf{q}\cdot(\mathbf{R}_{p}^{-}-\mathbf{R}_{p})} e_{\mathbf{q}} D_{\mathbf{q}}^{\mathrm{ph}} e_{\mathbf{q}}^{\dagger}$$

$$\tag{7}$$

where,  $w_{\mathbf{q}}$  denotes the weight of the  $\mathbf{q}$  points, and  $e_{\mathbf{q}}$  represent the orthogonal eigen value dynamical matrix. Subsequently, the electron-phonon matrix elements are given as,

$$g(\mathbf{R}_e, \mathbf{R}_p) = \frac{1}{N_p} \sum_{\mathbf{q}, \mathbf{k}} \omega_{\mathbf{k}} \omega_{\mathbf{q}} e^{-i(\mathbf{k} \cdot \mathbf{R}_e + \mathbf{q} \cdot \mathbf{R}_p)} U_{\mathbf{k} + \mathbf{q}}^{\dagger} g(\mathbf{k}, \mathbf{q}) U_{\mathbf{k}} \mathbf{u}_{\mathbf{q}}^{-1}$$
(8)

where,  $U_{\rm k}$  and  $U_{\rm k}+{\rm q}$  symbolize electronic matrices,  ${\bf u_q}$  denotes the phonon eigenvectors scaled by atomic masses, and  $N_p$  stands for the number of unit cells in the period supercell [84,85]. The rapid decay of all the quantities with distance in the electron or phonon unit cell is shown in Fig. S11. As the distance increases, all the quantities rapidly approach zero within the electron or phonon unit cells as shown in Fig. S11.

### CRediT authorship contribution statement

Pravin Karna: Writing – original draft, Methodology, Investigation, Formal analysis. Md Rafiqul Islam: Methodology. Eric R. Hoglund: Methodology, Writing – review & editing. Patrick E. Hopkins: Writing – review & editing, Resources, Project administration, Funding acquisition. Ashutosh Giri: Conceptualization, Supervision, Writing – original draft, Writing – review & editing, Resources, Project administration, Funding acquisition.

# Declaration of competing interest

The authors declare the following financial interests/personal relationships which may be considered as potential competing interests: Ashutosh Giri reports financial support and equipment, drugs, or supplies were provided by University of Rhode Island. If there are other authors, they declare that they have no known competing financial interests or personal relationships that could have appeared to influence the work reported in this paper.

## Data availability

Data will be made available on request.

# Acknowledgements

This manuscript is based upon work supported by the Office of Naval Research, Grant No. N0001421-1-2622, Air Force office of Scientific Research, Grant No. FA9550-22-1-0456 and the National Science Foundation, Grant Nos. CBET 2318576 and 2119365.

# Appendix A. Supplementary data

Supplementary data to this article can be found online at https://doi.org/10.1016/j.mtchem.2024.101991.

# References

- [1] J. Sinova, Nat. Mater. 9 (2010) 880.
- [2] G.E.W. Bauer, E. Saitoh, B.J. Van Wees, Nat. Mater. 11 (2012) 391.
- [3] P.B. Allen Bõidar, Theory of Superconducting T, 1982.
- [4] P.B. Allen, PHYSICAL REVIEW LETTERS Theory of Thermal Relaxation of Electrons in Metals, 1987.
- [5] Z. Zhang, I.D. Mayergoyz, J. Appl. Phys. 7 (2008) 07F510.
- [6] S.Y. Savrasov, D.Y. Savrasov, O.K. Andersen, YSICAL REVIEW LETTERS PH, Linear-response calculations of electron-phonon, Interactions 72 (1994) 372–375.
- [7] B. Liao, B. Qiu, J. Zhou, S. Huberman, K. Esfarjani, G. Chen, Phys. Rev. Lett. 114 (2015), https://doi.org/10.1103/PhysRevLett.114.115901.
- [8] P. Karna, A. Giri, Phys. Rev. B (2023) 107, https://doi.org/10.1103/ PhysRevB.107.094301.
- [9] Göran Grimvall, The Electron-Phonon Interaction in Metals, 1981.
- [10] W.L. Chan, R.S. Averback, D.G. Cahill, Appl. Phys. Mater. Sci. Process 97 (2009) 287.
- [11] W.L. Chan, R.S. Averback, D.G. Cahill, Y. Ashkenazy, Phys. Rev. Lett. 102 (2009), https://doi.org/10.1103/PhysRevLett.102.095701.
- [12] W.L. Chan, R.S. Averback, D.G. Cahill, A. Lagoutchev, Phys. Rev. B Condens. Matter 78 (2008), https://doi.org/10.1103/PhysRevB.78.214107.
- [13] D. Ivanov, L. Zhigilei, Phys. Rev. B Condens. Matter 68 (2003), https://doi.org/ 10.1103/PhysRevB.68.064114.
- [14] D. Gall, J. Appl. Phys. 119 (2016), https://doi.org/10.1063/1.4942216.

- [15] D. Gall, J. Appl. Phys. 127 (2020), https://doi.org/10.1063/1.5133671.
- [16] A.M. Brown, R. Sundararaman, P. Narang, W.A. Goddard, H.A. Atwater, ACS Nano 10 (2016) 957.
- [17] A.M. Brown, R. Sundararaman, P. Narang, A.M. Schwartzberg, W.A. Goddard, H. A. Atwater, Phys. Rev. Lett. 118 (2017), https://doi.org/10.1103/ PhysRevLett.118.087401.
- [18] H.A. Atwater, A. Polman, Nat. Mater. 9 (2010) 205.
- [19] R. Sundararaman, P. Narang, A.S. Jermyn, W.A. Goddard, H.A. Atwater, Nat. Commun. 5 (2014), https://doi.org/10.1038/ncomms6788.
- [20] C. Clavero, Nat. Photonics 8 (2014) 95.
- [21] J.D. Caldwell, L. Lindsay, V. Giannini, I. Vurgaftman, T.L. Reinecke, S.A. Maier, O. J. Glembocki, Nanophotonics 4 (2015) 44.
- [22] P. Drude, Ann. Phys. 308 (1900) 369.
- [23] S.D. Brorson, A. Kazeroonian, S. Moodera, D.W. Face, T.K. Cheng, E.P. Ippen, M. S. Dresselhaus, G. Dresselhaus, NUMBER 18 PHYSICAL REVIEW LETTERS, 1990.
- [24] M. Bonn, D.N. Denzler, S. Funk, M. Wolf, S.-S. Wellershoff, J. Hohlfeld, Ultrafast electron dynamics at metal surfaces: competition between electron-phonon coupling and hot-electron, Transport 61 (2000) 1101–1105.
- [25] J. Hohlfeld, S.-S. Wellershoff, J. Güdde, U. Conrad, V. Jahnke, E. Matthias, M. Matthias, Electron and Lattice Dynamics Following Optical Excitation of Metals, 2000.
- [26] S.I. Anisimov, L.D. Landau, B. Rethfeld, On the theory of ultrashort laser pulse interaction with a metal 3093 (1997) 192–203.
- [27] R.H.M. Groeneveld, R. Sprik, Effect of a Nonthermal Electron Distribution on the Electron-Phonon Energy Relaxation Process in Noble Metals, 1992.
- [28] A. Giri, J.T. Gaskins, B.M. Foley, R. Cheaito, P.E. Hopkins, J. Appl. Phys. 117 (2015), https://doi.org/10.1063/1.4906553.
- [29] Q. Wu, H. Zhou, Y. Wu, L. Hu, S. Ni, Y. Tian, F. Sun, F. Zhou, X. Dong, Z. Zhao, J. Zhao, Chin. Phys. Lett. 37 (2020), https://doi.org/10.1088/0256-307X/37/9/ 097802.
- [30] Z.Y. Tian, Q.Y. Zhang, Y.W. Xiao, G.A. Gamage, F. Tian, S. Yue, V.G. Hadjiev, J. Bao, Z. Ren, E. Liang, J. Zhao, Phys. Rev. B (2022) 105, https://doi.org/ 10.1103/PhysRevB.105.174306.
- [31] Y.C. Tian, W.H. Zhang, F.S. Li, Y.L. Wu, Q. Wu, F. Sun, G.Y. Zhou, L. Wang, X. Ma, Q.K. Xue, J. Zhao, Phys. Rev. Lett. 116 (2016), https://doi.org/10.1103/ PhysRevLett.116.107001.
- [32] Q. Wu, F. Sun, Q. Zhang, L.X. Zhao, G.F. Chen, J. Zhao, Phys. Rev. Mater. 4 (2020), https://doi.org/10.1103/PhysRevMaterials.4.064201.
- [33] W.S. Fann, R. Storz, H.W.K. Tom, J. Bokor, Electron thermalization in gold 46 (1992) 13592–13595.
- [34] W.S. Fann, R. Storz, H.W.K. Tom, J. Bokor, Direct measurement of nonequilibrium electron-energy distributions in subpicosecond laser-heated gold, Films 68 (1992) 2834–2837.
- [35] C.-K. Sun, F. Vallee, L.H. Acioli, E.P. Ippen, J.G. Fujimoto, Femtosecond-tunable measurement of electron thermalization in gold 50 (1994) 15337–15348.
- [36] S.D. Brorson, J.G. Fujimoto, E.P. Ippen, Femtosecond electronic heat-transport dynamics in thin gold films 59 (1987) 1962–1965.
- [37] S.I. Anisimov, B.L. Kapeliovich, T.L. Perelman, Sov. Phys. JETP 39 (1975) 375.
- [38] M.B. Agranat, S.I. Ashitkov, A.V. Ovchinnikov, D.S. Sitnikov, A.A. Yurkevich, O. V. Chefonov, L.T. Perel'man, S.I. Anisimov, V.E. Fortov, JETP Lett. 101 (2015) 598.
- [39] H. Petek, S. Ogawa, FEMTOSECOND TIME-RESOLVED TWO-PHOTON PHOTOEMISSION STUDIES OF ELECTRON DYNAMICS IN METALS, 1997.
- [40] S. Ishii, S.L. Shinde, T. Nagao, Adv. Opt. Mater. 7 (2019), https://doi.org/10.1002/adom.201800603.
- [41] J. Huang, W. Wang, C.J. Murphy, D.G. Cahill, Proc. Natl. Acad. Sci. U. S. A. 111 (2014) 906.
- [42] R.H.M Groeneveld, R. Sprik, A. Lagendijk, S. Uoor, Fundamenteel Onderzoek der Materie, Ultrafast Relaxation of Electrons Probed by Surface Plasmons at a Thin Silver, Film 64 (1990) 784.
- [43] B.C. Gundrum, R.S. Averback, D.G. Cahill, Appl. Phys. Lett. 91 (2007), https://doi. org/10.1063/1.2752731.
- [44] A. Rousse, C. Rischel, S. Fourmaux, I. Uschmann, S. Sebban, G. Grillon, P. Balcou, E. Fo, J.P. Geindre, P. Audebert, J.C. Gauthier, D. Hulin, Non-Thermal Melting in Semiconductors Measured at Femtosecond Resolution, 2001.
- [45] D.S. Ivanov, L.V. Zhigilei, Phys. Rev. Lett. 98 (2007), https://doi.org/10.1103/ PhysRevLett.98.195701.
- [46] D.S. Ivanov, A.I. Kuznetsov, V.P. Lipp, B. Rethfeld, B.N. Chichkov, M.E. Garcia, W. Schulz, Appl. Phys. Mater. Sci. Process 111 (2013) 675.
- [47] S.S. Wellershoff, J. Hohlfeld, J. Güdde, E. Matthias, Appl. Phys. Mater. Sci. Process 69 (1999), https://doi.org/10.1007/s003390051362.
- [48] J. Stingl, F. Zamponi, B. Freyer, M. Woerner, T. Elsaesser, A. Borgschulte, Phys. Rev. Lett. 109 (2012), https://doi.org/10.1103/PhysRevLett.109.147402.
- [49] A. Schiffrin, T. Paasch-Colberg, N. Karpowicz, V. Apalkov, D. Gerster, S. Mühlbrandt, M. Korbman, J. Reichert, M. Schultze, S. Holzner, J.V. Barth, R. Kienberger, R. Ernstorfer, V.S. Yakovlev, M.I. Stockman, F. Krausz, Nature 507 (2014) 386.
- [50] B. Nagler, U. Zastrau, R.R. Fäustlin, S.M. Vinko, T. Whitcher, A.J. Nelson, R. Sobierajski, J. Krzywinski, J. Chalupsky, E. Abreu, S. Bajt, T. Bornath, T. Burian, H. Chapman, J. Cihelka, T. Döppner, S. Düsterer, T. Dzelzainis, M. Fajardo, E. Förster, C. Fortmann, E. Galtier, S.H. Glenzer, S. Göde, G. Gregori, V. Hajkova, P. Heimann, L. Juha, M. Jurek, F.Y. Khattak, A.R. Khorsand, D. Klinger, M. Kozlova, T. Laarmann, H.J. Lee, R.W. Lee, K.H. Meiwes-Broer, P. Mercere, W. J. Murphy, A. Przystawik, R. Redmer, H. Reinholz, D. Riley, G. Röpke, F. Rosmej, K. Saksl, R. Schott, R. Thiele, J. Tiggesbäumker, S. Toleikis, T. Tschentscher, I. Uschmann, H.J. Vollmer, J.S. Wark, Nat. Phys. 5 (2009) 693.
- [51] L. Yuan, T. Wang, T. Zhu, M. Zhou, L. Huang, J. Phys. Chem. Lett. 8 (2017) 3371.

- [52] H. Liu, C. Wang, Z. Zuo, D. Liu, J. Luo, Adv. Mater. 32 (2020), https://doi.org/ 10.1002/adma.201906540.
- [53] S. Deng, E. Shi, L. Yuan, L. Jin, L. Dou, L. Huang, Nat. Commun. 11 (2020), https://doi.org/10.1038/s41467-020-14403-z.
- [54] Z. Guo, Y. Wan, M. Yang, J. Snaider, K. Zhu, L. Huang, Long-range hot-carrier transport in hybrid perovskites visualized by ultrafast microscopy 356 (2017) 59–62.
- [55] T. Wang, L. Jin, J. Hidalgo, W. Chu, J.M. Snaider, S. Deng, T. Zhu, B. Lai, O. Prezhdo, J.-P. Correa-Baena, L. Huang, Protecting Hot Carriers by Tuning Hybrid Perovskite Structures with Alkali Cations, 2020.
- [56] L. Yuan, T.-F. Chung, A. Kuc, Y. Wan, Y. Xu, Y.P. Chen, T. Heine, L. Huang, P H Y S I C S Photocarrier Generation from Interlayer Charge-Transfer Transitions in WS 2-Graphene Heterostructures, 2018.
- [57] T. Zhu, L. Yuan, Y. Zhao, M. Zhou, Y. Wan, J. Mei, L. Huang, P H Y S I C S Highly Mobile Charge-Transfer Excitons in Two-Dimensional WS 2/Tetracene Heterostructures, 2018.
- [58] M.M. Gabriel, J.R. Kirschbrown, J.D. Christesen, C.W. Pinion, D.F. Zigler, E. M. Grumstrup, B.P. Mehl, E.E.M. Cating, J.F. Cahoon, J.M. Papanikolas, Nano Lett. 13 (2013) 1336.
- [59] A. Block, M. Liebel, R. Yu, M. Spector, Y. Sivan, F.J. García De Abajo, N.F. Van Hulst, P.H. Tracking, Ultrafast Hot-Electron Diffusion in Space and Time by Ultrafast Thermomodulation Microscopy, 2019.
- [60] M. Segovia, X. Xu, Nano Lett. 21 (2021) 7228.
- [61] P. Karna, M.S. Bin Hoque, S. Thakur, P.E. Hopkins, A. Giri, Nano Lett. 23 (2023) 491
- [62] A. Block, R. Yu, I.W. Un, S. Varghese, M. Liebel, N.F. van Hulst, S. Fan, K. J. Tielrooij, Y. Sivan, ACS Photonics (2022), https://doi.org/10.1021/acsphotonics.2c01916.
- [63] A.M.J.S. Dugdale, Electrical Resistivity, Thermoelectrical Power and Optical Properties, Springer-Verlag, Berlin/Heidelberg, 1985.
- [64] Z. Tong, S. Li, X. Ruan, H. Bao, Phys. Rev. B 100 (2019), https://doi.org/10.1103/ PhysRevB.100.144306.
- [65] Y. Chen, J. Ma, S. Wen, W. Li, npj Comput. Mater. 5 (2019), https://doi.org/ 10.1038/s41524-019-0235-7.
- [66] A. Jain, A.J.H. McGaughey, Phys. Rev. B 93 (2016), https://doi.org/10.1103/ PhysRevB.93.081206.
- [67] S. Sæther, M.F. Erichsen, S. Xiao, Z. Zhang, A. Lervik, J. He, AIP Adv. (2022) 12, https://doi.org/10.1063/5.0094170.
- [68] N. Bhatt, P. Karna, S. Thakur, A. Giri, Phys. Rev. Mater. (2023) 7, https://doi.org/ 10.1103/PhysRevMaterials.7.115001.

- [69] K. Fladischer, V. Leitgeb, L. Mitterhuber, G.A. Maier, J. Keckes, M. Sagmeister, S. Carniello, S. Defregger, Thermochim. Acta (2019) 681, https://doi.org/ 10.1016/j.tca.2019.178373.
- [70] H. Butler, R.K. Williams, Electron-phonon interaction and lattice, Thermal Conductivity 18 (1978) 6483–6494.
- [71] S.Y. Savrasov, D.Y. Savrasov, Electron-Phonon Interactions and Related Physical Properties of Metals from Linear-Response Theory, 1996.
- [72] J.G. Fujimoto, J.M. Liu, E.P. Ippen, N. Bloembergen, Femtosecond laser interaction with metallic tungsten and nonequilibrium electron and lattice temperatures 53 (1984) 1837–1840.
- [73] R.H.M. Groeneveld, R. Sprik, A. Lagendijk, Femtosecond Spectroscopy of Electron-Electron and Electron-Phonon Energy Relaxation in Ag and Au, 1995.
- [74] J. Hohlfeld, J.G. Müller, S.-S. Wellershoff, E. Matthias, Rapid Communication Time-Resolved Thermoreflectivity of Thin Gold Films and its Dependence on Film Thickness. Springer-Verlag. 2024.
- [75] L. Guo, S.L. Hodson, T.S. Fisher, X. Xu, J. Heat Tran. 134 (2012), https://doi.org/ 10.1115/1.4005255.
- [76] Z. Lin, L.V. Zhigilei, V. Celli, Phys. Rev. B Condens. Matter 77 (2008), https://doi. org/10.1103/PhysRevB.77.075133.
- [77] A. Giri, P.E. Hokins, J. App. Phys. 118 (21) (2015).
- [78] R. Rosati, R. Perea-Causín, S. Brem, E. Malic, Nanoscale 12 (2020) 356.
- [79] A.M. Berghuis, T.V. Raziman, A. Halpin, S. Wang, A.G. Curto, J.G. Rivas, J. Phys. Chem. Lett. 12 (2021) 1360.
- [80] P. Giannozzi, S. Baroni, N. Bonini, M. Calandra, R. Car, C. Cavazzoni, D. Ceresoli, G.L. Chiarotti, M. Cococcioni, I. Dabo, A. Dal Corso, S. De Gironcoli, S. Fabris, G. Fratesi, R. Gebauer, U. Gerstmann, C. Gougoussis, A. Kokalj, M. Lazzeri, L. Martin-Samos, N. Marzari, F. Mauri, R. Mazzarello, S. Paolini, A. Pasquarello, L. Paulatto, C. Sbraccia, S. Scandolo, G. Sclauzero, A.P. Seitsonen, A. Smogunov, P. Umari, R.M. Wentzcovitch, J. Phys. Condens. Matter 21 (2009), https://doi.org/10.1088/0953-8984/21/39/395502.
- [81] S. Poncé, E.R. Margine, C. Verdi, F. Giustino, Comput. Phys. Commun. 209 (2016) 116.
- [82] N. Marzari, A.A. Mostofi, J.R. Yates, I. Souza, D. Vanderbilt, Rev. Mod. Phys. 84 (2012) 1419.
- [83] N. Troullier, J.L. Martins, Efficient Pseudopotentials for Plane-Wave Calculations-II. 1991.
- [84] U.C. Jesse, Berkeley UC Berkeley Electronic Theses and Dissertations Title the Electron-Phonon Interaction from First Principles, 2011.
- [85] F. Giustino, M.L. Cohen, S.G. Louie, Phys. Rev. B Condens. Matter 76 (2007), https://doi.org/10.1103/PhysRevB.76.165108.